

Generalization of parallel ghost imaging based on laboratory X-ray source

Nixi Zhao,^{1,2,3} Junxiong Fang,^{1,2,3} Jie Tang,^{1,2,3} Changzhe Zhao,^{1,2,3}
Jianwen Wu,^{1,2,3} Han Guo,² Haipeng Zhang,^{2*} and Tiqiao Xiao^{1,2,3,*}

¹*Shanghai Institute of Applied Physics, Chinese Academy of Sciences, Shanghai 201800, People's Republic of China*

²*Shanghai Synchrotron Radiation Facility/Zhangjiang Lab, Shanghai Advanced Research Institute, Chinese Academy of Sciences, Shanghai 201204, People's Republic of China*

³*University of Chinese Academy of Sciences, Beijing 100049, People's Republic of China*

*txiao@sari.ac.cn

*zhanghp@sari.ac.cn

Abstract: Ghost imaging (GI), as a novel imaging technique, facilitates image acquisition under low-light conditions through single-pixel measurements. Thus, it holds great potential in various application areas, such as biomedical imaging, remote sensing imaging, biometrics, astronomy, and three-dimensional imaging. However, to reconstruct high-resolution images, GI typically demands a large number of single-pixel samplings, which is extremely time-consuming and imposes practical limitations on its applications. Parallel ghost imaging treats each pixel of a position-sensitive detector as a bucket detector to perform tens of thousands of ghost imaging operations simultaneously in parallel. In our previous work, we have gradually achieved parallel ghost imaging with high pixel resolution, low dose, and an extra-large field of view. Parallel ghost imaging has demonstrated outstanding performance and vast potential. We were able to achieve pipeline-style imaging with an image size of 14000×10000 pixels and a pixel size of 0.65 μm within several minutes at a lower dose than that required for traditional projections. All of this is truly exciting. Nevertheless, all of our experiments were conducted at synchrotron radiation facilities. The almost unlimited and continuous light supply time, monochromatic, pure, and energy-tunable X-rays, expensive and precise experimental equipment, as well as complete supporting facilities—such a series of almost luxurious conditions make it impossible for many peers lacking experimental resources to replicate parallel ghost imaging. Meanwhile, the high cost also hinders its cross-disciplinary integration.

In this work, we broke away from synchrotron radiation facility and completed the pipeline-style acquisition of parallel ghost imaging using rough and inexpensive equipment in the most reproducible way for others. Eventually, we achieved ghost imaging with an effective pixel size of 8.03 μm , an image size of 2880×2280, and a minimum of 10 measurement numbers (a sampling rate of 0.62%) using a laboratory X-ray light source. We are absolutely confident in claiming that, in the field of X-ray ghost imaging, the reconstruction results of this work exhibit an unprecedented level of image quality and image size. Moreover, it can be achieved merely by making minor modifications to any industrial CT device. With a total experimental cost of only \$40, this work demonstrates great universality. We have put forward a comprehensive framework for the practical application of parallel ghost imaging, which is an essential prerequisite for the generalization of parallel ghost imaging to enter the commercial and practical arenas.

1. Introduction

The traditional imaging model primarily consists of three components: the light source, the object, and the optical system. In contrast, ghost imaging (GI), a novel imaging technique, employs a non-localized approach to separate detection from imaging. Ghost imaging involves splitting the light into two beams: one beam carries the object information but lacks resolution, while the other beam carries resolution but lacks object information. Neither beam alone is capable

of imaging, but by correlating the two beams computationally, the object information can be reconstructed. Hence, ghost imaging is also referred to as correlation imaging.

Ghost imaging originates from the Hanbury-Brown and Twiss (HBT) experiment [1, 2]. In 1988, Klyshko [3] theoretically proposed a ghost imaging scheme using entangled photon pairs. In 1994, Ribeiro et al. [4] discovered the phenomenon of ghost interference using entangled photon pairs. In 1995, Pittman et al. [5] experimentally demonstrated ghost imaging using entangled photon pairs. In 2002, Bennink et al. [6] realized ghost imaging with classical light sources, proving that entangled light sources are not a necessary condition for ghost imaging. Furthermore, ghost imaging has been shown to be feasible in various fields, including atomic [7], electronic [8], neutron [9, 10], and X-ray [11–15] imaging. In 2008, Shapiro [16] theoretically proposed a computational ghost imaging scheme, making single-channel ghost imaging possible. In 2009, Bromberg et al. [17] experimentally realized computational ghost imaging. In the same year, Katz et al. [18] integrated compressive sensing techniques from image processing with computational ghost imaging, significantly reducing the number of samples required for ghost imaging. This development made dose reduction in X-ray ghost imaging feasible. Moreover, ghost imaging has enormous potential across various application areas, including biomedical imaging [19], remote sensing [20], biometrics [21, 22], astronomy [23], and three-dimensional imaging [24, 25].

However, to reconstruct high-resolution images, Ghost imaging typically requires a large number of single-pixel samples, which poses challenges for its practical application. The concept of parallel ghost imaging (PGI) was introduced by Kingston et al. [9] to address this issue. This method treats each pixel of a position-sensitive detector as an independent bucket detector, enabling the simultaneous execution of tens of thousands of ghost imaging measurements at once. Kingston et al. and Zhang et al. successfully demonstrated PGI in neutron [9] and X-ray [26, 27], respectively. Later, O. Sefi et al. extended similar work to high-energy X-rays [28].

In our previous work, we established a true magnification configuration between the reference arm and the object arm using lenses, achieving high-pixel-resolution parallel imaging at the sub-micron level ($0.325\text{ }\mu\text{m/pixel}$) and increasing the experimental efficiency from dozens of minutes to just a few minutes [29]. Zhao et al. achieved low-dose ghost imaging by using two detectors in crystal-splitting ghost imaging. By constructing an extra-large speckle space, we realized ghost imaging with an extra-large field of view of 14000×10000 pixels [30]. We also specifically proposed global ghost imaging for the bucket detector array architecture, which can achieve high-quality reconstruction with an ultra-low sampling rate of only 8 measurements. Moreover, this method can eliminate the discontinuity between ghost imaging subsystems [31]. Subsequently, we replaced the crystal splitting with a computational ghost imaging framework to achieve low-dose ghost imaging, significantly improving the image quality and, for the first time, simultaneously realizing large-field-of-view, low-dose, and high-pixel-resolution ghost imaging [32].

However, the transformation of scientific research achievements has run into difficulties. All the above progress was completed relying on the Shanghai Synchrotron Radiation Facility. The nearly infinite and continuous light supply time, monochromatic, pure, and energy-adjustable X ray, expensive and precise experimental equipment, and the complete supporting facilities – this series of almost luxurious services provided by synchrotron radiation make it impossible for many peers lacking experimental conditions to replicate parallel ghost imaging. At the same time, the high cost has also hindered its cross-disciplinary integration.

In this work, we got rid of the synchrotron radiation source and completed the pipeline-style collection of parallel ghost imaging with rough and inexpensive equipment in the most imitable way. Eventually, with a laboratory X-ray source, we achieved ghost imaging with an effective pixel size of $8.03\text{ }\mu\text{m}$, an image size of 2880×2280 , and a minimum of 10 measurement numbers (a sampling rate of 0.62%). We are absolutely confident to claim that, in the field of X-ray ghost

imaging, the reconstruction results of this work have unparalleled image quality and image size. It can be achieved simply by placing copper foam(\$ 40) and a few sheets of sandpaper on the sample stage of any industrial CT device to enable movement, which endows this work with great universality. We have proposed a comprehensive framework, which is an essential prerequisite for the generalization of parallel ghost imaging to enter commercial and practical fields.

2. Methods, experiments and discussion

Model For the ghost imaging model from a classical perspective, the bucket detector signals acquired from N measurements in object arm can be written in the form of a matrix in Eq.1.

$$\begin{bmatrix} B_1 \\ B_2 \\ \vdots \\ B_N \end{bmatrix} = \begin{bmatrix} I_1(1,1) & I_1(1,2) & \cdots & I_1(p,1) & \cdots & I_1(p,q) \\ I_2(1,1) & I_2(1,2) & \cdots & I_2(p,1) & \cdots & I_2(p,q) \\ \vdots & \vdots & \vdots & \vdots & \vdots & \vdots \\ I_N(1,1) & I_N(1,2) & \cdots & I_N(p,1) & \cdots & I_N(p,q) \end{bmatrix} \begin{bmatrix} T(1,1) \\ T(1,2) \\ \vdots \\ T(p,q) \end{bmatrix} \quad (1)$$

The object's transmittance function $T(x, y)$, which contains internal structural information of the sample, is the unknown target we aim to reconstruct in ghost imaging. Both the image size of the mask and the reconstructed ghost image of samples are $p \times q$. The transmittance function of the k -th mask is denoted as $I_k(x, y)$, where $x = 1, \dots, p$ and $y = 1, \dots, q$, respectively. N represents the number of measurements, B_i denotes the bucket detector signal during the i -th measurement, and the sampling rate is defined as the number of measurements divided by the number of image pixels, i.e. $\frac{N}{p \times q}$. A higher sampling rate leads to higher quality of ghost imaging. For the detector in the object arm, the incident X-ray photons need to pass through the mask and subsequently through the object, which means that the absorption of both the mask and object should be taken into account. Ghost imaging, at its essence, is solving underdetermined linear equation set. PGI simply utilizes this process repeatedly for all the single pixels of the bucket detector array in the object arm, as shown in Fig.1.(b).

Algorithm PGI is based on the Total Variation Augmented Lagrangian Alternating Direction Algorithm [33] using compressive sensing. TVAL3 uses Total Variation Regularization (TV) as an iterative model:

$$\min_u \sum_i \|D_i u\|, \quad s.t. Au = b, \quad (2)$$

A is the speckle patterns, u is the image of the object to be solved, b is the measurements of the bucket detector, $D_i u$ is the gradient of u at pixel i , $\|\cdot\|$ is the $l1$ norm. The Augmented Lagrangian method transforms a constrained model into an unconstrained objective function, and then uses the Alternating Direction method to solve the objective function at high speed.

Experiment We take a complete industrial CT platform as the basic model for modification, enabling any research group capable of conducting X ray computed tomography to easily achieve high quality parallel ghost imaging. The laboratory light source we use is the micro focus X ray source (XWT - 225 The Plus) from X RAY WorX. It has a maximum voltage of 225 kV, a minimum voltage of 20 kV, a current range from 0.05 mA to 1 mA, a maximum emission power of 80 W, and a maximum target power of 50 W. It is a transmission type X ray tube. The target material consists of diamond and tungsten, with a radiation angle of 160° , and the resolution can reach the sub micron level. The detector is a CMOS camera (Teledyne DALSA Shad - o - Box 6K HS), which has 2940×2304 pixels, an effective area of $14.6 \text{ cm} \times 11.4 \text{ cm}$, and a resolution of $49.5 \mu\text{m}$.

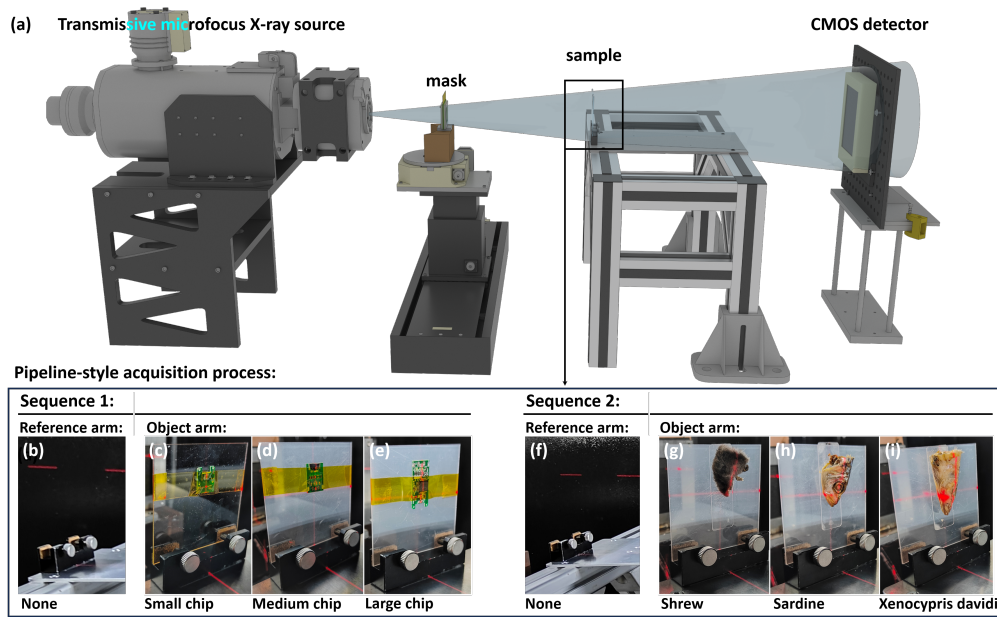


Fig. 1. (a) Schematic diagram of parallel ghost imaging based on a laboratory X ray tube. In the pipeline - style acquisition, the reference arm is collected first, followed by the object arm in each light supply cycle. When collecting the reference arm in cycle 1 (b) and cycle 2 (f), no object is placed. In the first cycle, we completed the collection of the objec arm for the small chip (c), medium sized chip (d), and large chip (e). In the second cycle, we completed the collection of the object arm for the shrew (g), sardine (h), and xenocypris davidi (i).

Regarding the motors, in the ghost imaging experiments at the synchrotron radiation facility, we built two sets of motor complexes for the mask and the object respectively to achieve high precision movement without human interference and vibration during the experiment. From the perspective of minimizing production costs, all these are unnecessary. The sample stage of a conventional CT platform is equipped with a rotation axis (R), a vertical movement axis (Z), and a horizontal movement axis (Y). For the movement of the mask, only the Y - axis is used to ensure that the speckles in the reference arm and the object arm are consistent. The function of the Z - axis, which is to adjust the height of the mask, is replaced by a flat piece of hardwood. The role of the R - axis is to adjust the mask to be completely perpendicular to the optical path so that the orthogonal basis speckles can be used in the experiment. We directly use cheap and easily accessible random speckles and thus abandon the R - axis. When the mask is not perpendicular to the optical path, the speckles will scale during movement, appearing larger when closer and smaller when farther away. Multiple experiments have verified that this does not affect the imaging quality for random speckles. Therefore, only one motor (Y - axis) is required to complete the experiment. We abandon all customized devices and directly use hot - melt glue to fix the hardwood, the mask, and the sample stage. Experiments have proven that the error is very small.

Pipeline - style In synchrotron radiation, we have achieved pipeline - based parallel ghost imaging. Both the mask and the object need to be able to move in and out of the optical path to collect flat field and dark field images. This is to eliminate the background caused by the hexagonal honeycomb structure of the detector scintillator, dark noise, and non - uniform X ray

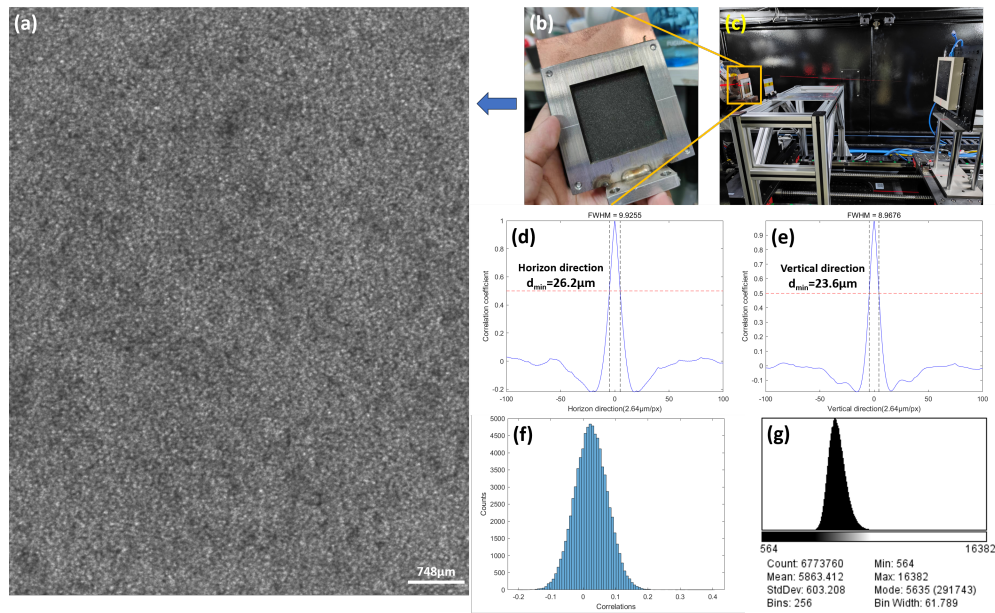


Fig. 2. Speckle Analysis. (a) Speckle pattern of the reference arm. (b) Physical image of the mask. (c) Physical image of the CT X ray machine. The full - width at half - maximum of the point spread function of the mask in the horizontal (d) and vertical (e) directions. (f) Correlation degree among speckles. (g) Modulation ability of the mask.

155 distribution. By taking advantage of the characteristic of ghost imaging that relies on second -
 156 order fluctuations for imaging, we normalize each group of object arm and reference arm data
 157 and subtract the mean value. This allows us to eliminate the background without collecting flat
 158 field and dark field images. Based on this, all the motors of the object - carrying stage can be
 159 removed, which further significantly reduces costs and paves the way for industrialization.

160 Ghost imaging demands temporal stability of light. However, unlike synchrotron radiation,
 161 which provides continuous, stable, and nearly unlimited illumination time, laboratory light sources
 162 can cause slight changes in the X ray distribution even when the light is switched on/off or the
 163 door is opened/closed. Long term illumination by a micro focus laboratory level light source
 164 can lead to a large number of electrons bombarding the target in the vacuum chamber, melting
 165 the target. It can only support continuous illumination for up to four hours. Even worse, after
 166 refocusing and resuming illumination, the X ray distribution can change significantly. Compared
 167 with experiments completed within the same cycle, the images reconstructed from the
 168 reference arm and object arm data collected before and after refocusing have higher noise, and
 169 the discontinuity between single - pixel subsystems is more prominent. From the perspective
 170 of industrialization and commercialization, it is necessary to efficiently measure a series of objects.
 171 Therefore, within each illumination cycle, we first perform high definition acquisition of
 172 the speckle pattern of the reference arm with an 8 s exposure time (Fig.1.(b) and (f)). Then, we
 173 sequentially carry out pipeline - style acquisition of the signals of the bucket detector array for
 174 different objects with a 0.1 s exposure time. First, we verify the success of applying parallel ghost
 175 imaging to laboratory light sources with cost - reduction and efficiency - enhancement using a
 176 set of chips (small chip in Fig.1.(c), medium - sized chip in Fig.1.(d), large chip in Fig.1.(e)).
 177 Then, in the second cycle, we challenge ourselves with low - contrast biological soft - tissue
 178 objects (shrew in Fig.1.(g), sardine in Fig.1.(h), Xenocypris davidi in Fig.1.(i)). A schematic

179 diagram of the experimental equipment is shown in Fig.1.(a).

180 **Speckle** The speckle pattern plays a decisive role in the reconstruction quality of ghost imag-
181 ing, as the resolution of the reconstruction result cannot be smaller than the minimum effective
182 feature of the speckle pattern. Generally speaking, smaller pixels in the reference arm detector
183 can capture higher density mask information, which implies better image quality. Larger pix-
184 els in the object arm detector can capture the encoded object information more quickly, which
185 means a lower radiation dose. The particle width of the mask cannot effectively describe the
186 minimum feature of the mask. Irregular particle edges, sharp densit gradient changes inside the
187 particles, and the superposition of multiple layers of random masks all make the minimum ef-
188 fective feature much smaller than the particle width. The modulation ability of the mask for X
189 ray is shown in Fig.2.(g). The point spread function (PSF), which is the autocovariance of the
190 mask pattern, is the soft upper limit of the resolution of the final imaging result of ghost imaging.
191 However, at a high sampling rate, the PSF can be surpassed. The full width at half maximum
192 (FWHM) of the PSF in the horizontal and vertical directions is shown in Fig.2.(d) and (e). If a
193 speckle can be linearly represented by the superposition of other speckle patterns, it is an invalid
194 measurement. The statistical histogram of the correlation degree of any combination of two
195 speckles (C_{400}^2) is shown in Fig.2.(f), which means that random speckles can be approximately
196 regarded as orthogonal to each other.

197 The physical diagram of the experiment is shown in Fig.2.(c). The energy range of the X ray
198 Imaging and Biomedical Application Beamline Station (BL13HB) of the Shanghai Synchrotron
199 Radiation Facility [34] is 0 - 40 keV. The energy of the micro focus X ray tube is much higher.
200 In the experiment, we used a voltage of 70 kV and a current of 120 mA, which means that the
201 output X ray energy spectrum is a continuous spectrum containing tungsten characteristic peaks
202 with a maximum electron energy of 70 keV. This has caused great difficulties in the parallel
203 ghost imaging experiment. The commonly used 7 layer sandpaper has a weak modulation effect
204 on light at such a high energy. According to simulation experiments, the degree of fluctuation
205 of structured illumination does not affect the image quality. However, in actual experiments,
206 various noises and errors cover the entire process. If the modulation ability is not much greater
207 than the noise, the reconstruction result will be submerged in the noise. Therefore, we adopted
208 a hybrid random mask consisting of 4 layers of 200 mesh sandpaper + a dense copper foam with
209 a 10 μm pore size + 3 layers of 200 mesh sandpaper, which increased the modulation ability of
210 the light field. The physical diagram of the hybrid mask is shown in Fig.2.(b). The only cost
211 for converting the CT X ray machine into a parallel ghost imaging experimental platform was
212 purchasing a 0.2 mm thick dense copper foam, which cost \$40 in total. The speckle pattern of
213 the reference arm is shown in Fig.2.(a). The discussion of the mask is not over yet. We will
214 mention it again in the discussion and analysis of the imaging results of biological tissues.

215 **Results** Finally, we reconstructed a series of results with an image size of 2880×2280 and an
216 equivalent pixel size of 8.03 μm in a pipeline - style. The object arm data was obtained through
217 artificial fitting, with a 40×40 pixel block regarded as a subsystem. The results of different
218 numbers of measurements / sampling rates are presented in sequence in Fig.3. Fig.3.(a), (l), (w)
219 and Fig.4.(a), (l), (w) were obtained by traditional direct projection imaging and are listed on
220 the far left as a reference. The experimental results show astonishing image quality, which has
221 never been seen in the field of X ray ghost imaging. The patterns on the chips can be clearly
222 distinguished, and the chip edges are sharp. The micro focus X ray tube does not produce the
223 interference fringes of the double crystal monochromator of the synchrotron radiation source,
224 nor does it have the periodic severe jitter in the accelerator. For high contrast objects, the image
225 quality presented by the laboratory X ray source is even better than that of synchrotron radiation,
226 and the discontinuity of the single pixel subsystems is very weak.

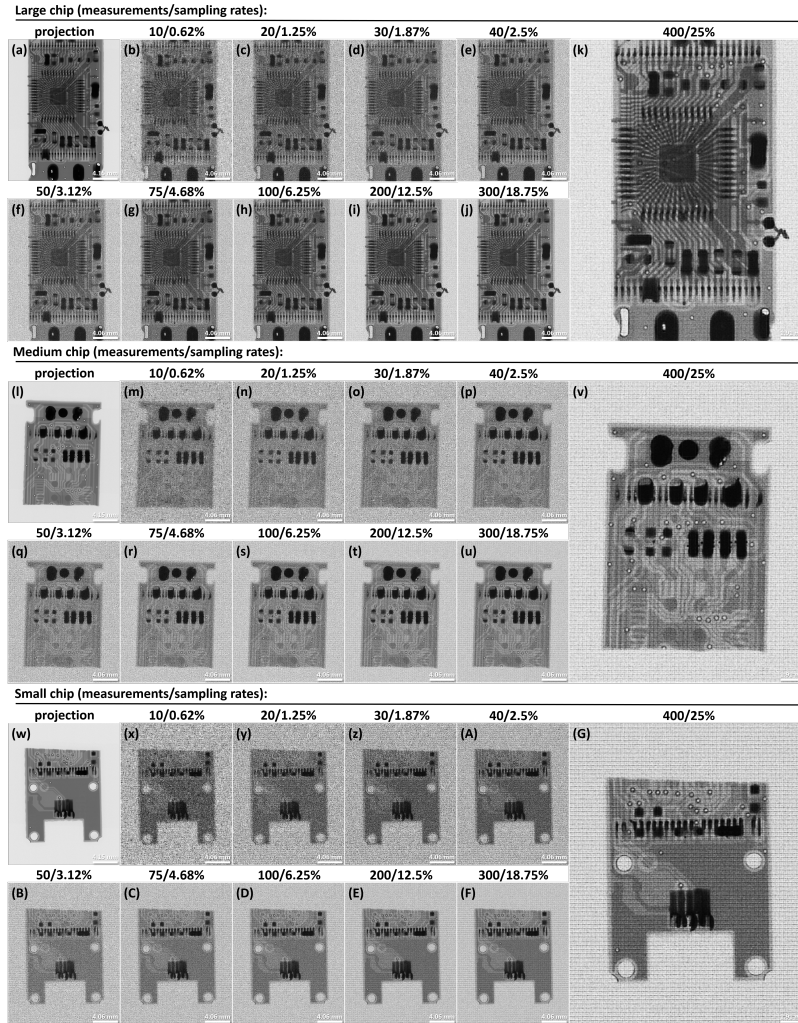


Fig. 3. The imaging results of the first cycle: For the small - sized chip sample, (a) is its projection imaging. The correspondence between the number of measurements / sampling rate and the results is as follows: (b) 10/0.62%, (c) 20/1.25%, (d) 30/1.87%, (e) 40/2.5%, (f) 50/3.12%, (g) 75/4.68%, (h) 100/6.25%, (i) 200/12.5%, (j) 300/18.75%, (k) 400/25%. For the medium - sized chip sample, (l) is its projection imaging. The correspondence between the number of measurements / sampling rate and the results is as follows: (m) 10/0.62%, (n) 20/1.25%, (o) 30/1.87%, (p) 40/2.5%, (q) 50/3.12%, (r) 75/4.68%, (s) 100/6.25%, (t) 200/12.5%, (u) 300/18.75%, (v) 400/25%. For the large - sized chip sample, (w) is its projection imaging. The correspondence between the number of measurements / sampling rate and the results is as follows: (x) 10/0.62%, (y) 20/1.25%, (z) 30/1.87%, (A) 40/2.5%, (B) 50/3.12%, (C) 75/4.68%, (D) 100/6.25%, (E) 200/12.5%, (F) 300/18.75%, (G) 400/25%.

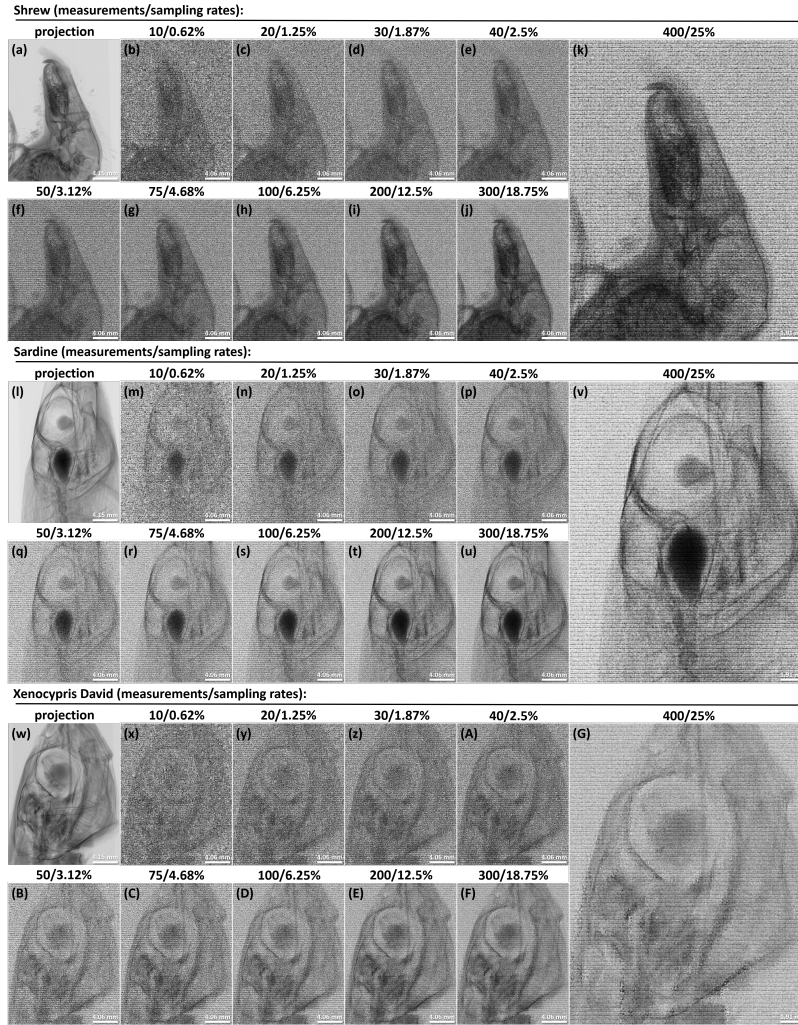


Fig. 4. The imaging results of the second cycle: For the shrew sample, (a) is its projection imaging. The correspondence between the number of measurements / sampling rate and the results is as follows: (b) 10/0.62%, (c) 20/1.25%, (d) 30/1.87%, (e) 40/2.5%, (f) 50/3.12%, (g) 75/4.68%, (h) 100/6.25%, (i) 200/12.5%, (j) 300/18.75%, (k) 400/25%. For the sardine sample, (l) is its projection imaging. The correspondence between the number of measurements / sampling rate and the results is as follows: (m) 10/0.62%, (n) 20/1.25%, (o) 30/1.87%, (p) 40/2.5%, (q) 50/3.12%, (r) 75/4.68%, (s) 100/6.25%, (t) 200/12.5%, (u) 300/18.75%, (v) 400/25%. For the xenocypris davidi sample, (w) is its projection imaging. The correspondence between the number of measurements / sampling rate and the results is as follows: (x) 10/0.62%, (y) 20/1.25%, (z) 30/1.87%, (A) 40/2.5%, (B) 50/3.12%, (C) 75/4.68%, (D) 100/6.25%, (E) 200/12.5%, (F) 300/18.75%, (G) 400/25%.

227 Then, in the second cycle, we further put the imaging capability of parallel ghost imaging for
 228 biological soft tissues to the test (Fig.4). Even in traditional projection imaging with an exposure
 229 time of 3 s, the part of the biological specimen with the weakest attenuation of high energy X rays
 230 only exhibits a contrast change of approximately 500 gray scale values. In parallel ghost imaging,
 231 the object arm acquisition uses an exposure time of only 0.1 s. This leads to a further weakening
 232 of the object signal, bringing it to a magnitude close to that of the ghost imaging noise, thus
 233 reducing the imaging quality. The vast and complex details of biological tissues slightly deviate
 234 from the sparse prior of TVAL3, which may also contribute to the degradation of the imaging
 235 effect. A decrease in the number of measurements or a reduction in the sampling rate implies
 236 a lower dosage and higher experimental efficiency. However, as the number of unknowns in
 237 the under determined equations increases, the image quality starts to decline. This downward
 238 trend does not seem to be linear. We attempted to uncover this pattern by using the Structural
 239 Similarity Index Measure (SSIM) between multiple samples at different sampling rates and the
 240 standard projection imaging. The corresponding graph is presented in Fig.5.(a). We discovered
 241 that, overall, the number of measurements and the imaging quality follow an logarithmic relation-
 242 ship. Once the number of measurements exceeds a certain threshold, its impact on the imaging
 243 quality becomes relatively minor. Meanwhile, an interesting phenomenon was observed: for all
 244 samples, the SSIM fluctuates when the number of measurements ranges from 30 to 50. Objects
 245 with higher contrast yield better imaging results. Additionally, the imaging quality of biological
 246 tissues can be effectively enhanced by increasing the number of measurements.

247 **True magnification** In this work, the bucket detector array of the object arm is obtained
 248 through artificial fitting, and the true magnification relationship between the object arm and
 249 the reference arm has not been successfully established. This means that the super resolution
 250 feature of ghost imaging has not been achieved, and thus the low dose and large field of view
 251 capabilities relying on super resolution cannot be realized either. We predict that there are three
 252 technical routes to achieve true magnification with laboratory light sources:

253 (1) Achieving true magnification by leveraging the cone beam property. The distances from
 254 the light outlet to the mask, the object, and the detector are 4.8 cm, 14.6 cm, and 90 cm respec-
 255 tively. The pixel size of the detector is 49.5 μm . This implies that the equivalent pixel size for the
 256 mask is $2.64 \mu\text{m} (\frac{4.8 \times 49.5}{90})$, and for the object is $8.03 \mu\text{m} (\frac{14.6 \times 49.5}{90})$, as shown in Fig.5.(b). We
 257 strikingly found that by using the magnification property of the cone beam, the true magnifica-
 258 tion correspondence between the object arm and the reference arm can be directly accomplished.
 259 We propose such a scenario: in the object arm, placing the detector as far forward as possible
 260 enlarges the field of view and the equivalent pixel size, reducing the dosage required for a single
 261 measurement. In the reference arm, placing the detector as far backward as possible reduces
 262 the field of view. Although the exposure time required for a single measurement is extremely
 263 long, it can achieve high resolution recording of the speckle pattern. Achieving true magnifica-
 264 tion using the cone beam property can eliminate the expensive optical lens group magnification
 265 system, demonstrating the excellent features of parallel ghost imaging, such as high resolution,
 266 large field of view, and low dose, at \$ 0 cost. This technique has great potential, and we will
 267 continue to work hard in this regard.

268 (2) Achieving pseudo magnification through artificial manipulation. We found that the artifi-
 269 cially fitted bucket detector array also seems to show a trend of reducing the dosage. The exposure
 270 time of the reference arm is 8 s, and the exposure times of the object arm are 8 s, 2 s, 0.5 s, 0.2 s,
 271 0.1 s, and 0.05 s. The reconstruction results corresponding to these exposure times, the speckle
 272 patterns of the object arm, and the gray value distributions of the object arm speckles are pre-
 273 sented in Fig.5.(d - i), (j - o), and (p - u) respectively. We found that the artificially fitted bucket
 274 detector array also meets the conditions for low light imaging. Even as the exposure time gradu-
 275 ally decreases and the dark field stripes exceed the object signal, the impact on the experimental

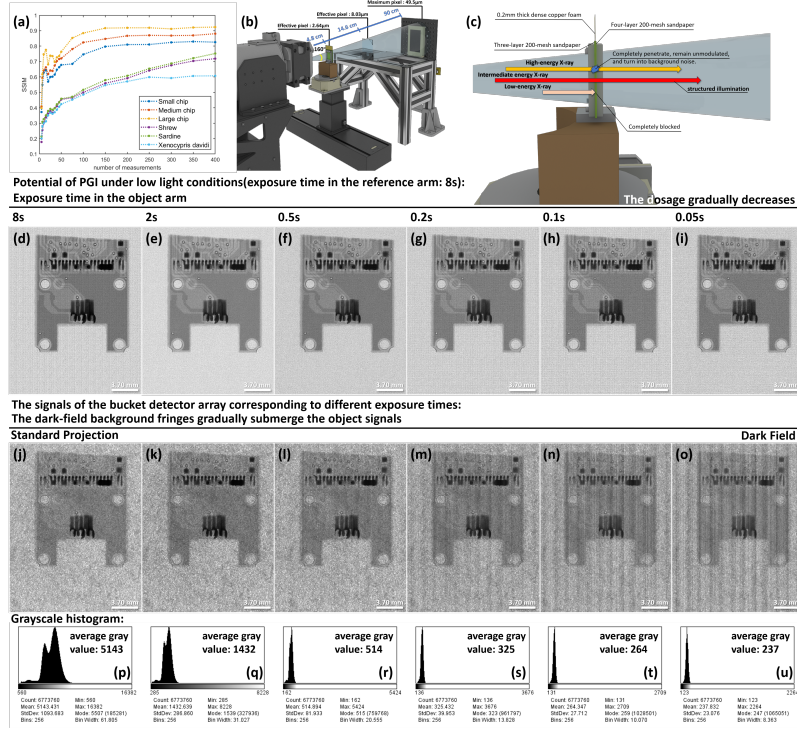


Fig. 5. (a) Curve chart of the structural similarity index measure comparing the reconstruction results at various sampling rates of the small chip, medium chip, large chip, shrew, sardine, and xenocypris davidi with their direct projections. (b) The characteristics of the cone beam of the laboratory light source make it possible to establish true magnification between the object arm and the reference arm at \$ 0 cost. (c) The interaction between white light and the mask. Low energy X rays are completely blocked by the mask, while high energy X rays completely penetrate the mask. Using a noiseless single photon detector holds the possibility of achieving low dose parallel ghost imaging. The exposure time of the reference arm is 8 s in all cases. The exposure time of the object arm gradually decreases ((j) 8 s, (k) 2 s, (l) 0.5 s, (m) 0.2 s, (n) 0.1 s, and (o) 0.05 s). However, the quality of the corresponding reconstruction results ((d) 8 s, (e) 2 s, (f) 0.5 s, (g) 0.2 s, (h) 0.1 s, and (i) 0.05 s) only deteriorates slightly. The grayscale histograms corresponding to different exposure times are presented in (p - u) to demonstrate that the collected object signals are indeed decreasing gradually.

276 results remains minimal. From Fig.5.(r), (s), (t), and (u), we can see that due to the background
277 noise of the detector, as the exposure time further decreases, the gray value of the object sig-
278 nal becomes smaller while the noise distribution remains unchanged. The object information is
279 masked by the noise, causing the reconstruction results to deteriorate. If we use a single photon
280 detector, which has no background noise and a high frame rate, it is theoretically possible to
281 achieve low dose imaging with the artificially fitted bucket detector array. Using an artificially
282 fitted single photon bucket detector array to reduce the dosage can also avoid the registration
283 problem that has not been solved in true magnification. We will explore the feasibility of this
284 direction in the future.

285 (3) Directly using a large pixel detector for the object arm and a small pixel detector for the
286 reference arm, and registering the two can achieve true magnification. This method can also be
287 combined with method (1) to further increase the magnification ratio.

288 **White Light** The white light emitted by the laboratory light source has an X ray energy range
289 spanning from 0 to 70 keV. The imaging challenges and phenomena it gives rise to are worthy
290 of discussion. For high energy X rays, the mask is completely penetrated, and no effective
291 modulation occurs. Moreover, the background noise generated by these photons that do not
292 participate in imaging bombarding the detector degrades the imaging quality. This is manifested
293 in the absence of pixels with lower gray values in Fig.2.(g) and Fig.5.(p). As for low energy X
294 ray photons, they are either completely blocked by the mask or can only slightly penetrate the
295 mask, generating scattered stray light that introduces noise into the imaging process. In parallel
296 ghost imaging with a laboratory X ray tube, the main imaging contribution comes from medium
297 energy X ray photons. These photons are effectively modulated by the mask to form structured
298 illumination for ghost imaging, as shown in the schematic diagram in Fig.5.(c). Different target
299 materials, voltages, as well as the thickness, type, and aperture size of the mask, will all lead
300 to different proportions of X rays that are either completely penetrated or completely blocked.
301 The presence of white light implies a significant need for mask customization. Systematically
302 researching, developing, customizing, and analyzing the optimal mask for various scenarios is
303 essential.

304 3. Conclusion

305 In summary, we first gradually achieved the three characteristics of high pixel resolution, extra
306 large field of view, and ultra low dose in parallel ghost imaging at the synchrotron radiation
307 facility. We also proposed global ghost imaging for the bucket detector array. With the gradual
308 improvement of parallel ghost imaging, it holds great application potential and commercial value.
309 Therefore, it is necessary to extract this technology from synchrotron radiation. In this work, we
310 have generalized parallel ghost imaging using a laboratory X ray source. We transformed a CT X
311 ray machine at the lowest cost (\$ 40) and through a method that is most easily replicated by peers,
312 and achieved pipeline style parallel ghost imaging with an image size of 2880×2280 and a pixel
313 resolution of 8.03 μm . The ghost imaging quality demonstrated in this work is unprecedented
314 in XGI. We proposed this parallel ghost imaging framework and believe it will point the way for
315 the practical application and commercialization of ghost imaging.

316 However, there are still many issues that urgently need to be addressed. Firstly, true magni-
317 fication based on the X ray tube has not been achieved yet. We are simultaneously working on
318 this technical barrier from the three proposed routes. Secondly, the resolution of parallel ghost
319 imaging is still far from the theoretical expectation. We are attempting to solve the registration
320 problem between the reference arm and the object arm to further improve the resolution.

321 At present, the development of parallel ghost imaging will branch into two main directions.
322 Starting from this work, parallel ghost imaging based on a mobile X ray tube will target the
323 medical imaging field and attempt to achieve high quality, large field of view ghost tomography

(GT). GT means that it can detect patients' lesions with a dose that is dozens to hundreds of times lower than that of conventional medical CT. This route aims to be convenient and affordable, and ultimately replace CT, thus having great commercial value. The other route of parallel ghost imaging will continue to develop at the synchrotron radiation facility, following a high end scientific research path. It will attempt to achieve imaging with nanometer level resolution and centimeter level field of view, filling the gap in this scientific research niche.

Funding. The National Key Research and Development Program of China (Grant Nos. 2022YFA1603601, 2021YFF0601203, 2021YFA1600703), the Young Scientists Fund of the National Natural Science Foundation of China (Grant No.12205361)

Acknowledgment. The authors thank WenJie Hao, Kang Du, Zenghao Song, JunXiong Fang, YanLing Xue, Ke Li and FeiXiang Wang for their kind help and fruitful discussion on experiments and data processing.

Disclosures. The authors declare no conflicts of interest.

Data Availability Statement. Data underlying the results presented in this paper are not publicly available at this time but may be obtained from the authors upon reasonable request.

References

1. R. Hanbury Brown and R. Q. Twiss, "A test of a new type of stellar interferometer on sirius," in *A Source Book in Astronomy and Astrophysics, 1900–1975*, (Harvard University Press, 1979), pp. 8–12.
2. R. H. Brown and R. Q. Twiss, "Correlation between photons in two coherent beams of light," *Nature* **177**, 27–29 (1956).
3. D. Klyshko, "Two-photon light: influence of filtration and a new possible epr experiment," *Phys. Lett. A* **128**, 133–137 (1988).
4. P. S. Ribeiro, S. Pádua, J. M. Da Silva, and G. Barbosa, "Controlling the degree of visibility of young's fringes with photon coincidence measurements," *Phys. Rev. A* **49**, 4176 (1994).
5. T. B. Pittman, Y. Shih, D. Strekalov, and A. V. Sergienko, "Optical imaging by means of two-photon quantum entanglement," *Phys. Rev. A* **52**, R3429 (1995).
6. R. S. Bennink, S. J. Bentley, and R. W. Boyd, "'two-photon' coincidence imaging with a classical source," *Phys. review letters* **89**, 113601 (2002).
7. R. I. Khakimov, B. Henson, D. Shin, *et al.*, "Ghost imaging with atoms," *Nature* **540**, 100–103 (2016).
8. S. Li, F. Cropp, K. Kaba, *et al.*, "Electron ghost imaging," *Phys. review letters* **121**, 114801 (2018).
9. A. M. Kingston, G. R. Myers, D. Pelliccia, *et al.*, "Neutron ghost imaging," *Phys. Rev. A* **101**, 053844 (2020).
10. Y.-H. He, Y.-Y. Huang, Z.-R. Zeng, *et al.*, "Single-pixel imaging with neutrons," *Sci. Bull.* **66**, 133–138 (2021).
11. H. Yu, R. Lu, S. Han, *et al.*, "Fourier-transform ghost imaging with hard x rays," *Phys. review letters* **117**, 113901 (2016).
12. D. Pelliccia, A. Rack, M. Scheel, *et al.*, "Experimental x-ray ghost imaging," *Phys. review letters* **117**, 113902 (2016).
13. A. Schori and S. Shwartz, "X-ray ghost imaging with a laboratory source," *Opt. express* **25**, 14822–14828 (2017).
14. D. Pelliccia, M. P. Olbinado, A. Rack, *et al.*, "Towards a practical implementation of x-ray ghost imaging with synchrotron light," *IUCrJ* **5**, 428–438 (2018).
15. A. Schori, D. Borodin, K. Tamasaku, and S. Shwartz, "Ghost imaging with paired x-ray photons," *Phys. Rev. A* **97**, 063804 (2018).
16. J. H. Shapiro, "Computational ghost imaging," *Phys. Rev. A—Atomic, Mol. Opt. Phys.* **78**, 061802 (2008).
17. Y. Bromberg, O. Katz, and Y. Silberberg, "Ghost imaging with a single detector," *Phys. Rev. A—Atomic, Mol. Opt. Phys.* **79**, 053840 (2009).
18. O. Katz, Y. Bromberg, and Y. Silberberg, "Compressive ghost imaging," *Appl. Phys. Lett.* **95** (2009).
19. Q.-B. Lu, L. Ding, Y.-Y. Zhou, *et al.*, "Ultrasonic holographic ghost imaging," *Phys. Rev. Appl.* **17**, 034052 (2022).
20. B. I. Erkmen, "Computational ghost imaging for remote sensing," *JOSA A* **29**, 782–789 (2012).
21. F. Lin, L. Hong, H. Guo, *et al.*, "Ghost identification for qr codes and fingerprints with thermal light modulation," *Phys. Rev. Appl.* **18**, 054060 (2022).
22. S. Yuan, D. Chen, X. Liu, and X. Zhou, "Optical encryption based on biometrics and single-pixel imaging with random orthogonal modulation," *Opt. Commun.* **522**, 128643 (2022).
23. D. V. Strekalov, B. I. Erkmen, and N. Yu, "Ghost imaging of space objects," in *Journal of Physics: Conference Series*, vol. 414 (IOP Publishing, 2013), p. 012037.
24. A. M. Kingston, D. Pelliccia, A. Rack, *et al.*, "Ghost tomography," *Optica* **5**, 1516–1520 (2018).
25. A. M. Kingston, G. R. Myers, D. Pelliccia, *et al.*, "X-ray ghost-tomography: Artefacts, dose distribution, and mask considerations," *IEEE Trans. on Comput. Imaging* **5**, 136–149 (2018).

- 380 26. H. Zhang, K. Li, F. Wang, *et al.*, “Megapixel x-ray ghost imaging with a binned detector in the object arm,” *Chin.*
381 *Opt. Lett.* **20**, 033401 (2022).
- 382 27. C.-Z. Zhao, H.-P. Zhang, J. Tang, *et al.*, “X-ray ghost imaging with a specially developed beam splitter,” *Synchrotron*
383 *Radiat.* **31** (2024).
- 384 28. O. Sefi, A. Ben Yehuda, Y. Klein, *et al.*, “20 μm resolution multipixel ghost imaging with high-energy x-rays,” *Opt.*
385 *Express* **32**, 37001–37010 (2024).
- 386 29. N. Zhao, J. Tang, C. Zhao, *et al.*, “Synthetic aperture x-ray ghost imaging with sub-micron pixel resolution,” *Opt.*
387 *Express* **33**, 972–982 (2025).
- 388 30. N. Zhao, J. Tang, C. Zhao, *et al.*, “Parallel ghost imaging with extra large field of view and high pixel resolution,”
389 *ChinaXiv* (2025).
- 390 31. N. Zhao, C. Zhao, J. Tang, *et al.*, “Global ghost imaging,” *ChinaXiv* (2025).
- 391 32. N. Zhao, J. Tang, C. Zhao, *et al.*, “Parallel ghost imaging with ultra low dose and high pixel resolution,” *ChinaXiv*
392 (2025).
- 393 33. C. Li, W. Yin, H. Jiang, and Y. Zhang, “An efficient augmented lagrangian method with applications to total variation
394 minimization,” *Comput. Optim. Appl.* **56**, 507–530 (2013).
- 395 34. J.-F. Ji, H. Guo, Y.-L. Xue, *et al.*, “The new x-ray imaging and biomedical application beamline bl13hb at ssrf,”
396 *Nucl. Sci. Tech.* **34**, 197 (2023).